

A Universal Destriping Framework Combining 1-D and 2-D Variational Optimization Methods

Xinxin Liu, Huanfeng Shen[✉], Senior Member, IEEE, Qiangqiang Yuan[✉], Member, IEEE, Xiliang Lu, and Chunging Zhou

Abstract—Striping effects are a common phenomenon in remote-sensing imaging systems, and they can exhibit considerable differences between different sensors. Such artifacts can greatly degrade the quality of the measured data and further limit the subsequent applications in higher level remote-sensing products. Although a lot of destriping methods have been proposed to date, a few of them are robust to different types of stripes. In this paper, we conduct a thorough feature analysis of stripe noise from a novel perspective. With regard to the problem of striping diversity and complexity, we propose a universal destriping framework. In the proposed destriping procedure, a 1-D variational method is first designed and utilized to estimate the statistical feature-based guidance. The guidance information is then incorporated into 2-D optimization to control the image estimation for a reliable and clean output. The iteratively reweighted least-squares method and alternating direction method of multipliers are exploited in the proposed approach to solve the minimization problems. Experiments under various cases of simulated and real stripes confirm the effectiveness and robustness of the proposed model in terms of the qualitative and quantitative comparisons with other approaches.

Index Terms—Destriping, mean cross-track profile, remote-sensing image, universal framework, variational optimization.

I. INTRODUCTION

AS TWO of the most commonly employed optical imaging technologies in remote-sensing systems, whiskbroom sensors (across-track scanning) and pushbroom sensors (along-track scanning) often acquire images that are contaminated with stripes. The main cause of such effects is the inconsistent responses among different sensors [1]. However, other factors,

including imperfect relative calibration, the response variation of the detectors, bright target saturation, and random noise, also contribute [2], [3]. Stripes, including the possible signal-dependent stripes [4], [5], can lead to significant uncertainties in the primary reflectance or radiance data. Without correction, these uncertainties will be concentrated and magnified in the higher level remote-sensing products, which would bring further problems in the data applications. Therefore, the correction of image stripes, which is commonly called “image destriping,” is crucial.

Due to the various impacts of different remote-sensing sensors, the features of stripe noise vary considerably. Here, we summarize six features of stripes in remote-sensing data: direction, degradation, distribution, periodicity, pattern, and persistence (short for 3-D-3P). To give a clear description, the detailed information is shown in Table I. All the illustrations are from real remote-sensing images.

The most understandable feature is direction, which further contains *horizontal*, *vertical*, and *oblique* components. As a result of the combination of the along-track placed sensor array and the across-track forward and reverse scanning [3], *horizontal* stripes generally appear in the images acquired by whiskbroom sensors. Some typical examples are the Multi-spectral Scanner, Landsat Thematic Mapper, and Moderate Resolution Imaging Spectroradiometer (MODIS). In contrast, instruments such as the High Resolution Visible instrument onboard the *Satellite Pour l’Observation de la Terre* satellite, the Hyperion sensor onboard EO-1, and many other high-resolution sensors adopt a pushbroom technique. In pushbroom scanning, since every image line is recorded along the track through an across-track placed array [1], *vertical* stripes are easily generated. In general, stripes are either *horizontal* or *vertical* in the original remote-sensing images. However, once georectification is performed, *oblique* stripes can appear.

The second feature, degradation, describes how severely a scan is contaminated. It can be classified into two categories: *warm* and *dead*. *Warm* scans are those scans that are brighter or darker than the healthy scans [6]. As a result, information about the ground objects can still remain in these stripes. However, *dead* scans, which are mainly caused by faulty detectors with a zero or constant response, contain no useful information as their inner pixels have no correlation with the true scene [7].

To introduce the distribution situation of stripes in the whole image, we use *local*, *global*, and *all* to detail the grades in the distribution feature. The *local* grade means that the

Manuscript received January 17, 2017; revised June 23, 2017 and September 10, 2017; accepted September 14, 2017. This work was supported by the National Natural Science Foundation of China under Grant 41401383, Grant 11471253, Grant 91630313, and Grant 41661134015. (Corresponding author: Huanfeng Shen.)

X. Liu and H. Shen are with the Beijing Advanced Innovation Center for Imaging Technology, Capital Normal University, Beijing 100048, China, and also with the School of Resource and Environmental Sciences, Wuhan University, Wuhan 430079, China (e-mail: yuki_lxx@126.com; shenhf@whu.edu.cn).

Q. Yuan is with the School of Geodesy and Geomatics, Wuhan University, Wuhan 430079, China (e-mail: yqiang86@gmail.com).

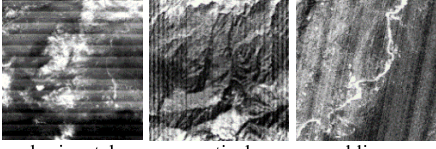

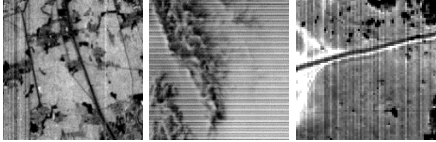
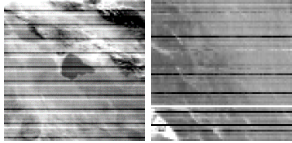
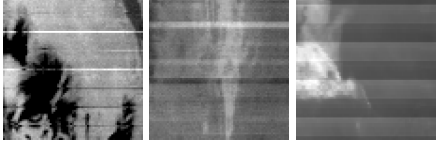
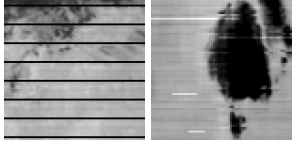
X. Lu is with the School of Mathematics and Statistics, Wuhan University, Wuhan 430072, China, and also with the Hubei Key Laboratory of Computational Science, Wuhan University, Wuhan 430072, China (e-mail: xllv.math@whu.edu.cn).

C. Zhou is with the Beijing Advanced Innovation Center for Imaging Technology, Capital Normal University, Beijing 100048, China (e-mail: zcp1688@sina.com).

Color versions of one or more of the figures in this paper are available online at <http://ieeexplore.ieee.org>.

Digital Object Identifier 10.1109/TGRS.2017.2755016

TABLE I
FEATURE ANALYSIS FOR STRIPE NOISE IN REAL DATA

Feature	Illustration
Direction	 horizontal vertical oblique
Degradation	 warm dead
Distribution	 local global all
Periodicity	 periodic non-periodic
Pattern	 single agminated banding
Persistence	 integral partial

stripes are concentrated in certain regional scans. Caused by the ill responses from a part of detectors, this grade can be found mainly in pushbroom images, since whiskbroom sensors reflect the influence of ill responses into the whole image through a repeating forward and reverse scanning mode. Conversely, the *global* grade, which can appear in pushbroom and even more often in whiskbroom images, describes a distinct situation where the stripes are widely distributed in the entire swath. Being the severest grade, *all* is a very special *global* distribution, since, in such a case, *all* the scans appear to be stripes and are difficult to distinguish as healthy information.

Closely related to the scanning mode, periodicity is another feature. In general, *nonperiodic* stripes are the most common and can be found in sensors with different kinds of scanning modes. In contrast, *periodic* stripes with much more regular structures always appear with the whiskbroom sensors, as a result of across-track scanning [8].

The fifth feature is pattern. *Single*, as the simplest pattern, describes stripe noise with a one-pixel width. *Agminated* denotes a different situation when a group of neighboring scans are simultaneously affected by stripes. *Banding* caused by sudden change in the bias level is a special case of an *agminated* pattern, with alternating bright and dark scans [3]. A typical example is the so-called mirror-side stripes in MODIS data, since a quasi-constant offset occurs during their forward and reverse scanning [2].

Finally, the persistence feature gives an apparent description about whether or not the stripe extends in a whole scan line. Even though most stripes belong to *integral*, *partial* stripes can be found in some images. For example, in specific thermal bands of MODIS images [2], stripes may appear with random lengths. The main cause of these partial stripes is unstable detectors whose sensitivity varies in a part of the scan during the scanning process [9].

From the above analyses, it can be seen that the stripe situation in remote-sensing images is very complicated. Furthermore, even in a single image, a mixture of different types of stripes is very common. Although many different destriping methods have been developed to date, a few of them can successfully deal with all different cases of stripes. In this paper, we propose a universal destriping model for remote-sensing images via joint usage of 1-D and 2-D variational methods. More specifically, a rough estimation of the mean statistics is first obtained through a 2-D optimization as guidance information, and is then employed to set up a 2-D destriping model. To efficiently solve the minimization problem, the iteratively reweighted least-squares (IRLS) and alternating direction method of multiplier (ADMM) methods are applied in the proposed approach. Various cases of stripe noise covering nearly all the features were tested in our experiments to validate the robustness of the proposed method.

The remainder of this paper is organized as follows. Section II gives a review of the previous destriping methods. Section III introduces the proposed variational model. The experimental results, along with a quantitative evaluation, are given in Section IV. Section V provides a further discussion on the proposed approach. Finally, we make a summary in Section VI.

II. REVIEW OF DESTRIPIING METHODS

Before acquiring remote-sensing images, their inner stripes are generally preprocessed according to the calibration coefficients computed either through the uniform light source in the laboratory (preflight) or onboard the satellite (in-flight) [10]. However, this preprocessing does not always work due to the imperfect calibration and/or the variability in the sensor response. Thus, image-based destriping techniques are also needed. In the literature, various methods have been explored to remove stripe noise from remotely sensed images. Based on their underlying similarity, we make a more detailed classification of these methods.

The first family of destriping approaches is the scene-based techniques. The main idea in this approach is to compute the relative relations between different detectors using selected stable scenes, or “flat-field” targets, before correcting the

other images. For instance, Fischer *et al.* [10] utilized stable scene images to obtain correction coefficients for hyperspectral SWIR data, supposing that the sensor conformed to a linear response; Corsini *et al.* [11] made use of a polynomial model to estimate equalization curves from homogeneous or quasi-homogeneous targets for final modular optoelectronic scanner image correction; Bindschadler and Choi [12] drew support from ice-sheet images to estimate the detector errors in Hyperion data. However, since the valid coefficients can change with the specific scene contents [10], scene-based methods can easily produce artifacts when using a fixed set of coefficients.

Filter-based methods, such as the Fourier domain filter [13], [14] wavelet analysis [15], [16], and the combined wavelet-Fourier filter [17], [18], are, to some extent, the most direct techniques. These methods work by analyzing and truncating the specific stripe component in a transformed domain, and hold the advantage of being able to process the georectified images [13], [16]. Since the periodic feature of stripes can be easily identified in a power spectrum analysis, the filtering-based methods are generally suitable for periodic stripes. However, the useful information can sometimes be filtered out along with the stripes if they possess the same frequency, which further results in significant blurring and/or ringing artifacts [13]–[15]. To overcome this limitation, Munch *et al.* [17] and Pande-Chhetri and Abd-Elrahman [18] have tried to find more accurate ways of stripe information truncation.

Another category of destriping technique, the interpolation-based methods, first ensures the stripe locations and then replaces the stripe pixels with reasonable values calculated by a designed interpolation function [9], [19]. These methods are simple, efficient, and robust for “single” pattern stripes, especially when their degradation is “dead” [9]. However, a main restriction of these methods is the stripe thickness [19], that is, interpolation is not possible when the width of the stripe noise is too large. Moreover, the stripe detection may also be intractable when faced with complex striped images [8], [19].

Statistical-based approaches constitute another popular destriping group. These methods examine the distribution of the digital numbers for each sensor and then adjust the target distribution to the reference one [3], [20]. Equalization methods [21], histogram modification [22], [23], and moment matching (MM) [20] are typical examples. Relatively speaking, the statistical-based approaches are the most widely utilized, because they have a better balance between efficacy and efficiency. However, their limitation is also nonneglectable, since these models simply consider that the response of each detector is invariable in the whole striping line, which is not always true in a real case. To improve the robustness, Rakwatin *et al.* [3] combined histogram matching with a facet filter for stripe noise reduction in MODIS data, and Shen *et al.* [24] proposed a piecewise approach based on local statistics. Nevertheless, the universality is still a problem.

Recently, optimization-based models have attracted much attention. Shen and Zhang [6] first proposed the Huber–Markov variational algorithm for the destriping problem. Carfantan and Idier [1] designed a calibration-related

model, which utilizes a maximum *a posteriori* framework to estimate the stripe multiplicative component, assuming that the additive component can be eliminated easily onboard. Unlike the detector response degradation model requiring an invariable calibration coefficient along the whole striping line, Bouali and Ladjal [2] employed a more flexible assumption by directly regarding stripes as additive noise (with different values in different pixels), and proposed a sophisticated algorithm after analyzing and modeling the directional structural information of the stripe noise. Subsequently, Chang *et al.* [25] further incorporated the sparse representation theory for the joint denoising and destriping problem. Paying special attention to the noise distribution, Liu *et al.* [26] designed a stripe noise separation model based on the latent sparsity of stripes in data. Furthermore, for highly dense stripes, Liu *et al.* [27] also proposed a variational model based on the statistical properties of the stripes. Optimization-based models are very promising because they produce good results in terms of both quantitative and qualitative evaluations. However, in addition to the efficiency problem, the optimization-based methods also have much room to improve their estimation when faced with different types of stripes.

Considering the high spectral correlation among different bands [28]–[30], there have also been some special methods developed for hyperspectral data. Sun *et al.* [31] proposed a spectral moment method for hyperspectral images by fully using the abundant spectral information. Acito *et al.* [4] exploited the orthogonal subspace approach to estimate the striping component and then remove it from the image. By using low-rank representation, Lu *et al.* [32] applied this framework to the hyperspectral image destriping problem, while Zhang *et al.* [33] focused on mixed noise removal. Driven by the unmixing theory [34], [35], Cerra *et al.* [36] designed an unmixing-based method for hyperspectral destriping and inpainting. Although some of these methods have the ability to simultaneously process other types of noise, when processing images with just a few more spectral bands, the computation time can greatly increase.

III. DESTRIPIING MODEL

A. Problem Formulation

Assuming that we have a clean true remote-sensing image and the striping effects are considered to be additive noise [2], [8], [25], then the degradation model can be described as

$$\mathbf{Y} = \mathbf{X} + \mathbf{S} \quad (1)$$

where \mathbf{Y} is the observed image and \mathbf{X} is the latent true image. The term \mathbf{S} denotes different kinds of stripe noise and minor random noise. Since the destriping task in this paper is to estimate the latent true image from the observation, the key becomes further exploring appropriate prior information to tackle this typical inverse problem. Although other degradation models may involve the specific response of the detectors, the more general assumption for stripe noise in (1) can be a much better fit for the complicated cases, enhancing the flexibility of the relevant destriping framework.

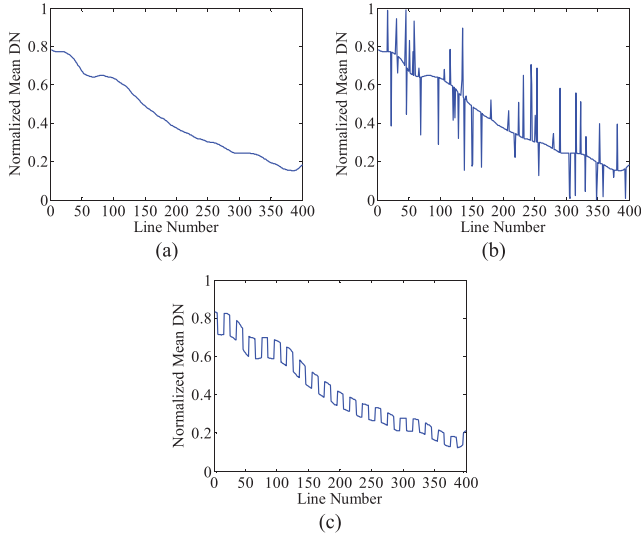


Fig. 1. Mean cross-track profiles in (a) normal image, (b) stripe-added image with “single” pattern stripes, and (c) stripe-added image with “banding” pattern stripes.

B. One-Dimensional Variational Optimization for the Desired Mean Cross-Track Profile

Stripe noise possesses a remarkable structural characteristic, which reflects in an obvious difference between striping lines and nonstriping lines in their along-stripe statistics. Taking a mean cross-track profile [13], [20], [24] as an example, the profile in the normal noise-free image is relatively smooth, as shown in Fig. 1(a). However, after adding the simulated structural stripes to the image, the profiles of both “single” pattern stripes and “banding” pattern stripes can become much more turbulent, as shown in Fig. 1(b) and (c). In general, in a real destriping case, the only known profile is the one with stripes. At this time, if the stripe-free desired mean cross-track profile is also available, then the calibration of the striping lines can be wholly controlled using this information as guidance. Hence, for an accurate destriping solution, the acquisition of the guided profile is very useful. Inspired by the above idea, we put guidance estimation in the first place and realize it via 1-D optimization of the mean cross-track profile.

Since the desired profile is much smoother but has a similar tendency to the stripe-affected one, by using the known noisy profile as the input, we can regard the estimation of the desired profile as a typical 1-D denoising problem [37]–[40]. As in the common variational methods, our data fidelity term is constructed to minimize the differences between the real and the desired profiles, while the regularization term is designed to ensure the smoothness of the estimated output. For the convenience of description, we assume that only horizontal stripes are displayed in $\mathbf{Y} \in \mathbf{R}^{m \times n}$ (m rows and n columns). However, for the vertical stripes, they can also be processed through a first rotation of the image matrix by 90° . The proposed model is defined as

$$\hat{\mathbf{g}} = \arg \min \left\{ \frac{1}{p} \|\mathbf{g} - \mathbf{Y}\mathbf{f}\|_p^p + \frac{\lambda}{2} \|\mathbf{D}\mathbf{g}\|_2^2 \right\} \quad (2)$$

where $p \in (0, 2]$, $\mathbf{f} \in \mathbf{R}^{n \times 1}$ is a column vector whose elements are equivalent to $1/n$, $\mathbf{g} \in \mathbf{R}^{m \times 1}$ represents the filtered result, λ tunes the smoothness of the estimated profile, and \mathbf{D} is a regularization matrix. Here, we choose \mathbf{D} as a blur matrix corresponding to the blur kernel $[1 \ -2 \ 1]^T$. It can be easily seen that $\mathbf{Y}\mathbf{f}$ calculates the original noisy mean cross-track profile in \mathbf{Y} . In addition, the choice of the ℓ^p norm is aimed at treating different profiles in varying striping cases. For example, when stripe noise just occurs in several image lines, $p = 1$ will fit better than $p = 2$. Due to the fact that the Hodrick–Prescott filter (HP filter, commonly used in economics) [37], [38] is a fixed $p = 2$ model, which belongs to a special case of (2), our variational method can also be considered to be an enhanced generic HP filter.

Given that $p \in (0, 2]$ in (2) is an arbitrary value, we employ the IRLS method [1], [41], [42] to solve the problem. For each iteration, one needs to solve a weighted least-squares minimization

$$\hat{\mathbf{g}}^{(k+1)} = \arg \min \left\{ \frac{1}{2} \|\mathbf{W}^{(k)1/2}(\mathbf{g} - \mathbf{Y}\mathbf{f})\|_2^2 + \frac{\lambda}{2} \|\mathbf{D}\mathbf{g}\|_2^2 \right\} \quad (3)$$

where

$$\mathbf{W}^{(k)} = \text{diag}(\mathcal{T}(\mathbf{g}^{(k)} - \mathbf{Y}\mathbf{f})) \quad (4)$$

and

$$\mathcal{T}(x) = \begin{cases} |x|^{p-2}, & \text{if } |x| > \alpha \\ \alpha^{p-2}, & \text{if } |x| \leq \alpha \end{cases} \quad (5)$$

for a small positive α .

Therefore, $\hat{\mathbf{g}}^{(k+1)}$ has a closed-form solution as

$$\hat{\mathbf{g}}^{(k+1)} = (\mathbf{W}^{(k)} + \lambda \mathbf{D}^T \mathbf{D})^{-1} \mathbf{W}^{(k)} \mathbf{Y}\mathbf{f}. \quad (6)$$

C. 2-D Variational Optimization for the Destriped Image

As a typical inverse problem, destriping needs prior knowledge to constrain its solution space for a more accurate estimation. Therefore, after obtaining the filtered profile as the solution of (2), denoted by $\hat{\mathbf{g}}(\mathbf{Y})$ hereafter, we introduce this destriping guidance in our model and construct the constraint term as

$$G(\mathbf{X}) = \|\hat{\mathbf{g}}(\mathbf{Y}) - \mathbf{X}\mathbf{f}\|_2^2. \quad (7)$$

By penalizing the differences between the filtered profile and the profile in the desired data through an ℓ^2 norm, $G(\mathbf{X})$ can effectively keep the consistency in the recovered data from the guidance information, and functions to further control the destriping process for a reliable output.

To smooth the image noise under an optimization-based framework, the effectiveness of total variation (TV)-based techniques has been proved in many applications [2], [6], [8], [43]–[45]. In [6], we successfully removed the stripe noise by employing the isotropic finite second-order differences. However, considering the obvious directional characteristics of the stripe noise, an unsymmetrical regularization would be more adaptive. As a consequence, anisotropic TV regularization [2] is thus chosen

$$R(\mathbf{X}) = \|\nabla_h \mathbf{X} - \nabla_h \mathbf{Y}\|_1 + \lambda_1 \|\nabla_v \mathbf{X}\|_1 \quad (8)$$

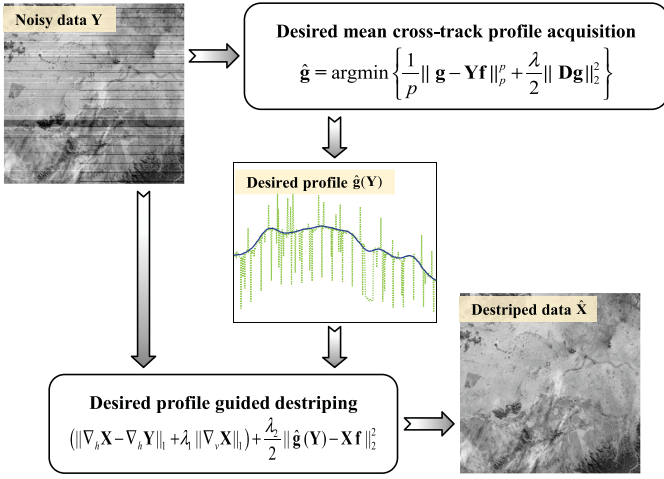


Fig. 2. Flowchart of the proposed universal destripping framework.

where ∇_h and ∇_v separately denote the partial differential operator in the along-stripe and across-stripe directions and λ_1 is the parameter controlling the functioning degree of these two terms. In $R(\mathbf{X})$, $\|\nabla_h \mathbf{X} - \nabla_h \mathbf{Y}\|_1$ maps the along-stripe gradients from the observed \mathbf{Y} to the desired \mathbf{X} , aiming at maintaining the stripe-unaffected gradients in \mathbf{X} , while $\|\nabla_v \mathbf{X}\|_1$ acts as the key term to suppress the stripe noise via minimizing the across-stripe gradients in the desired image.

Finally, a unified destripping framework is proposed by combining the statistical feature-based guidance $G(\mathbf{X})$ with the anisotropic regularization $R(\mathbf{X})$ as follows:

$$\hat{\mathbf{X}} = \arg \min E(\mathbf{X}) \quad (9)$$

where

$$E(\mathbf{X}) = R(\mathbf{X}) + \frac{\lambda_2}{2} G(\mathbf{X}) = (\|\nabla_h \mathbf{X} - \nabla_h \mathbf{Y}\|_1 + \lambda_1 \|\nabla_v \mathbf{X}\|_1) + \frac{\lambda_2}{2} \|\hat{g}(\mathbf{Y}) - \mathbf{Xf}\|_2^2 \quad (10)$$

where λ_2 is the parameter used to balance the anisotropic regularization and the statistical feature-based guidance. In the proposed model, the calculation of the guidance never needs extra information from other data, so it can be self-estimated for all the images as long as their stripes extend horizontally or vertically. In addition, all the stripes must meet the anisotropic property. Therefore, the proposed model holds good universality and can be expected to work in all horizontally and vertically striped images. The framework of the proposed method is illustrated in Fig. 2.

The difficulty in solving the proposed model (10) mainly lies in the nondifferentiability and inseparability of the ℓ^1 -norm terms. Since the ADMM approach can decouple the nonsmooth ℓ^1 term from the smooth loss term, which is computationally efficient [46], it is a great choice to tackle this problem. We therefore apply the ADMM principle to minimize this cost function. By introducing two auxiliary variables \mathbf{H} and \mathbf{V} , the unconstrained minimization problem (10) can

be converted into a constrained one

$$\min \left\{ \|\mathbf{H}\|_1 + \lambda_1 \|\mathbf{V}\|_1 + \frac{\lambda_2}{2} \|\hat{g}(\mathbf{Y}) - \mathbf{Xf}\|_2^2 \right\} \quad (11)$$

s.t. $\mathbf{H} = \nabla_h \mathbf{X} - \nabla_h \mathbf{Y}$, $\mathbf{V} = \nabla_v \mathbf{X}$.

As in the method of multipliers, the augmented Lagrangian is formed as follows:

$$\begin{aligned} \mathcal{L}(\mathbf{H}, \mathbf{V}, \mathbf{X}, p_1, p_2) &= \|\mathbf{H}\|_1 + \lambda_1 \|\mathbf{V}\|_1 + \frac{\lambda_2}{2} \|\hat{g}(\mathbf{Y}) - \mathbf{Xf}\|_2^2 \\ &+ p_1^T (\nabla_h \mathbf{X} - \nabla_h \mathbf{Y} - \mathbf{H}) + p_2^T (\nabla_v \mathbf{X} - \mathbf{V}) \\ &+ \frac{\rho_1}{2} \|\nabla_h \mathbf{X} - \nabla_h \mathbf{Y} - \mathbf{H}\|_2^2 + \frac{\rho_2}{2} \|\nabla_v \mathbf{X} - \mathbf{V}\|_2^2 \end{aligned} \quad (12)$$

where p_1 and p_2 are Lagrange multipliers and ρ_1 and ρ_2 denote the penalty parameters, which also control the step sizes for the update of their corresponding Lagrange multipliers. To solve (12), an alternating scheme is utilized, which decomposes the original problem into \mathbf{H} , \mathbf{V} , and \mathbf{X} , three simpler subproblems.

Note that both the \mathbf{H} -related and \mathbf{V} -related subproblems are decoupled, so their optimal values can be explicitly computed using a shrinkage operator [47]. We simply compute

$$\mathbf{H}^{k+1} = \text{shrink} \left(\nabla_h \mathbf{X}^k - \nabla_h \mathbf{Y} + \frac{p_1^k}{\rho_1}, \frac{1}{\rho_1} \right) \quad (13)$$

$$\mathbf{V}^{k+1} = \text{shrink} \left(\nabla_v \mathbf{X}^k + \frac{p_2^k}{\rho_2}, \frac{\lambda_1}{\rho_2} \right) \quad (14)$$

where *shrink* is the soft-shrinkage operator

$$\text{shrink}(r, \zeta) = \max(r - \zeta, 0) * \frac{r}{|r|}. \quad (15)$$

The \mathbf{X} -related subproblem is a quadratic minimization problem and equivalent to the linear system

$$\begin{aligned} \rho_1 \nabla_h^T \nabla_h \mathbf{X}^{k+1} + \rho_2 \nabla_v^T \nabla_v \mathbf{X}^{k+1} - \lambda_2 \mathbf{X}^{k+1} \mathbf{f}^T \\ = \rho_1 \nabla_h^T \left(\nabla_h \mathbf{Y} + \mathbf{H}^{k+1} - \frac{p_1^k}{\rho_1} \right) + \rho_2 \nabla_v^T \left(\mathbf{V}^{k+1} - \frac{p_2^k}{\rho_2} \right) \\ - \lambda_2 \hat{g}(\mathbf{Y}) \mathbf{f}^T \end{aligned} \quad (16)$$

which can be efficiently solved by the fast Fourier transform (FFT) due to its block-circulant structure [48].

In each iteration, the Lagrange multipliers p_1 and p_2 are finally updated by

$$\begin{cases} p_1^{k+1} = p_1^k + \rho_1 (\nabla_h \mathbf{X}^{k+1} - \nabla_h \mathbf{Y} - \mathbf{H}^{k+1}) \\ p_2^{k+1} = p_2^k + \rho_2 (\nabla_v \mathbf{X}^{k+1} - \mathbf{V}^{k+1}). \end{cases} \quad (17)$$

Combining (13), (14), (16), and (17), we have a one-step iteration for the ADMM. The optimization procedure of the proposed destripping model is summarized in Algorithm 1.

IV. EXPERIMENTAL RESULTS

Both simulated and real-data experiments were conducted to demonstrate the effectiveness of the generic destripping framework. The four comparative methods were as follows:

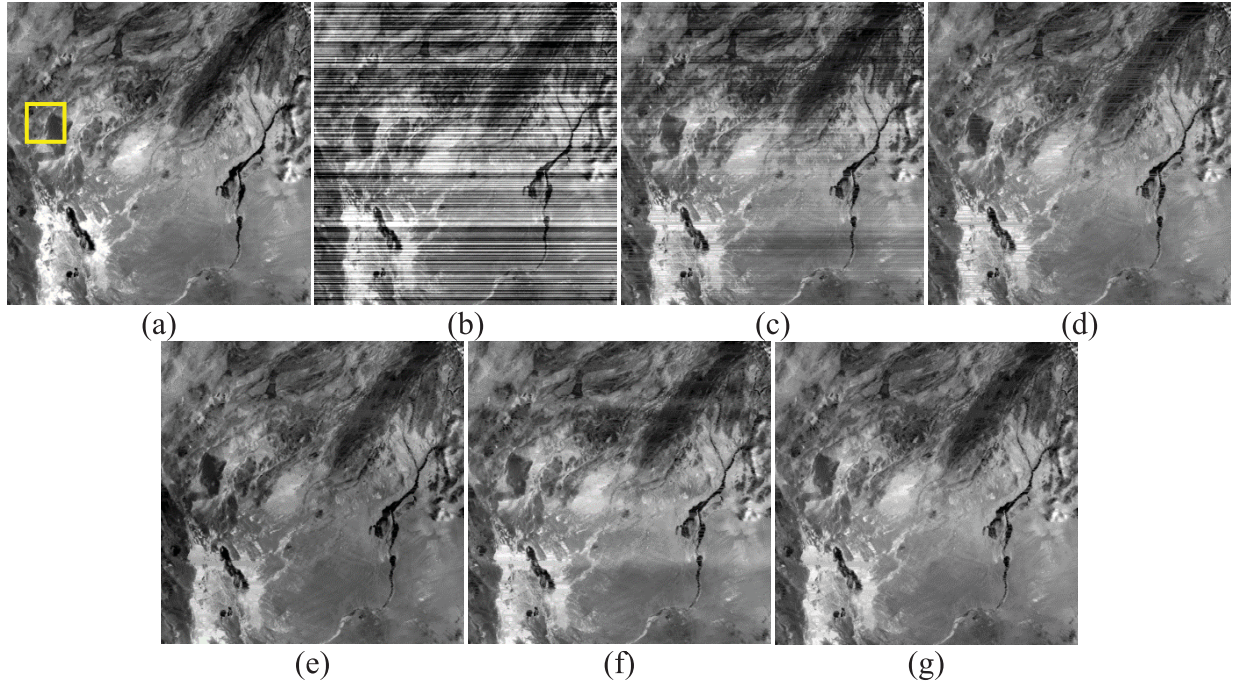


Fig. 3. Destriping results for simulated case 1. (a) Clean observation. (b) Degraded image. (c) MM. (d) WAFT. (e) UTV. (f) SSC. (g) Proposed method.

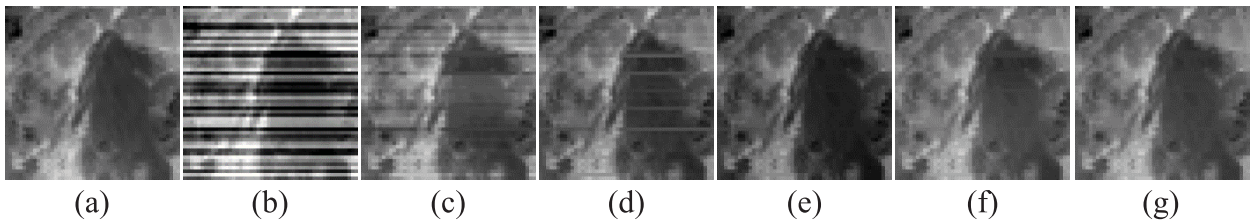


Fig. 4. Close-ups of the yellow rectangle marked region in Fig. 3. (a) Clean observation. (b) Degraded image. (c) MM. (d) WAFT. (e) UTV. (f) SSC. (g) Proposed method.

Algorithm 1 Proposed Destriping Algorithm

Input: data \mathbf{Y} , filtered profile $\hat{\mathbf{g}}(\mathbf{Y})$, and parameters $\lambda_1, \lambda_2, \rho_1, \rho_2$.

Initialize: $\mathbf{X}_0 = \mathbf{Y}, \mathbf{H}_0 = \mathbf{0}, \mathbf{V}_0 = \nabla_v \mathbf{Y}, p_1 = \mathbf{0}, p_2 = \mathbf{0}$, and $\varepsilon = 10^{-5}$

While ($\|\mathbf{X}^k - \mathbf{X}^{k-1}\| / \|\mathbf{X}^k\| > \varepsilon$ and $k < N_{\max}$) **do**

Solve $\mathbf{H}^{k+1}, \mathbf{V}^{k+1}$ using a thresholding method by (13), (14)

Compute \mathbf{X}^{k+1} ; the solution of (16) using FFT

Update the two Lagrange multipliers p_1^{k+1}, p_2^{k+1} by (17)

End While

Output: \mathbf{X}^{k+1}

- 1) MM [20];
- 2) combined wavelet-Fourier filtering (WAFT) [17];
- 3) the unidirectional TV model (UTV) [2];
- 4) the striping sparsity considered model (SSC) [26].

To allow a fair quantitative evaluation, all the test images were normalized between $[0, 1]$.

A. Simulated Data Experiments

As simulations, two very different striping cases were simulated by adding distinct stripe noise to the clean observations. The observation extracted from a heterogeneous area of Terra MODIS data with a size of 400×400 was utilized to simulate case 1. In this case, nearly all the image lines had stripe noise added, and the degradation levels among the striping lines were random, as shown in Fig. 3(b). In case 2, the observation was cut in a 400×400 homogeneous area from Aqua MODIS data. To make this case more different and complicated, both integral stripes and partial stripes were randomly and periodically simulated in the test image, respectively. In addition, a special agminated stripe with the width of 15 lines was also added, as shown in Fig. 5(b).

Figs. 3 and 4 compare the performance of stripe removal in case 1. Figs. 5 and 6 present the destriping results for simulated case 2. From Figs. 3–6, it can be clearly seen that the proposed destriping framework adequately alleviate the stripe noise, no matter if it is dense or sparse, partial or integral, single or agminated, and it can also preserve most of the detailed information from the clean observations. The parameters of the proposed model were set as $p = 2, \lambda = 125000$, and $\lambda_1 = 0.2$

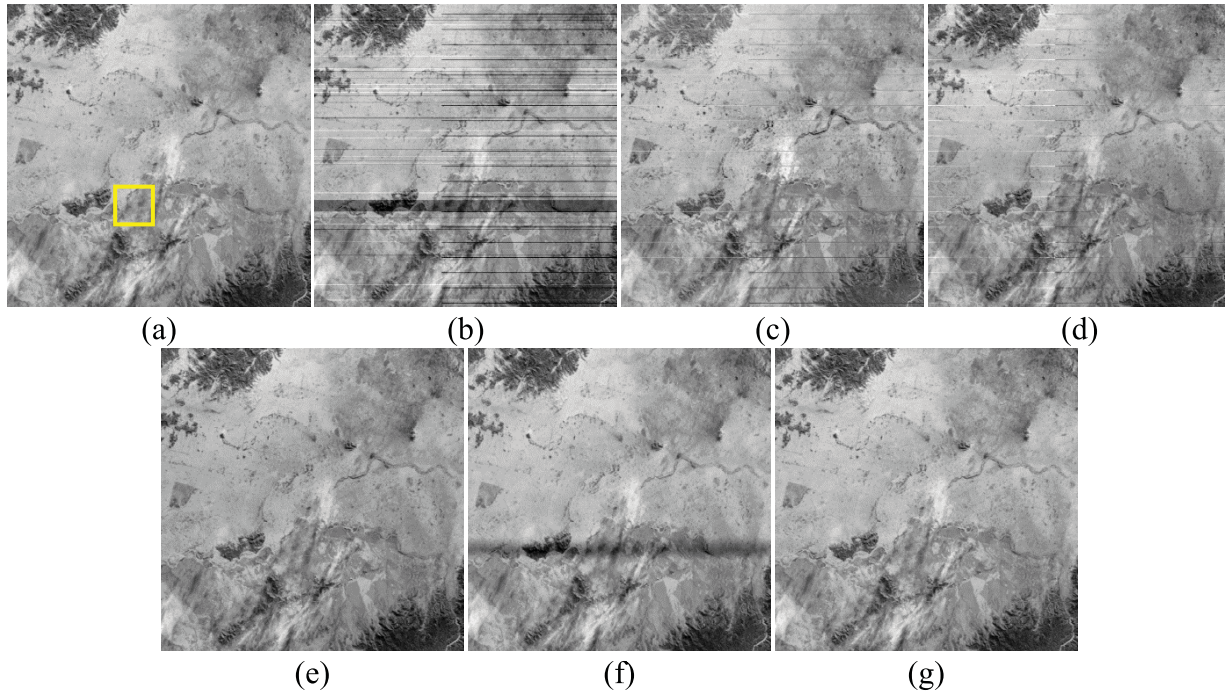


Fig. 5. Destriping results for simulated case 2. (a) Clean Observation. (b) Degraded image. (c) MM. (d) WAFT. (e) UTV. (f) SSC. (g) Proposed method.

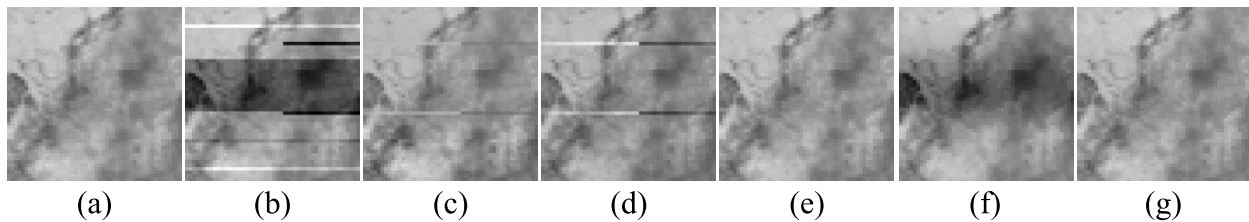


Fig. 6. Close-ups of the yellow rectangle marked region in Fig. 5. (a) Clean observation. (b) Degraded image. (c) MM. (d) WAFT. (e) UTV. (f) SSC. (g) Proposed method.

for case 1, and $p = 1$, $\lambda = 220000$, and $\lambda_1 = 0.1$ for case 2. Unlike the results of the proposed model, the results of MM and WAFT contain obvious unprocessed or over-processed stripes, and these are much more obvious in the close-ups. Although UTV can thoroughly remove the stripe noise, the brightness distortion in Fig. 4(e) reveals its drawback of possible oversmoothing. Based on the sparse assumption, the SSC method is able to remove the stripes in some relatively sparsely distributed regions, but, when faced with the dense case or when the stripes are too wide to be thought of as dense, its results become worse, as shown in Figs. 3(f) and 6(f).

Figs. 7 and 8 show the mean cross-track profiles in the two simulated cases. As expected, the red profiles output by the proposed method are much smoother than those from the corresponding noisy images (the green profile) and, more importantly, they are also the most similar to the blue reference profiles from the original stripe-free data. Moreover, the profiles of the proposed method after 1-D filtering and 2-D destriping are very similar, which essentially reflects the ability of the proposed model to adequately use the guidance information in the destriping process.

With the access to the ground truth, four full-reference indexes and two nonreference indexes were employed in the

simulated data experiments to give the quantitative evaluation. Among them, the improvement factor (IF1) [11], the peak signal-to-noise ratio (PSNR), the structural similarity (SSIM) index [49], [50], and the mean absolute error (MAE) are full-reference indexes. The definitions of these four indexes are as follows:

$$\text{IF}_1 = 10 \log_{10} \left(\frac{\sum_j (m_Y[j] - m_X[j])^2}{\sum_j (m_{\hat{X}}[j] - m_X[j])^2} \right) \quad (18)$$

$$\text{PSNR} = 10 \log_{10} \left(\frac{MN}{\|\hat{\mathbf{X}} - \mathbf{X}\|^2} \right) \quad (19)$$

$$\text{SSIM} = \frac{(2m_X m_{\hat{X}} + C_1)(2\sigma_{\mathbf{X}\hat{\mathbf{X}}} + C_2)}{(m_X^2 + m_{\hat{X}}^2 + C_1)(\sigma_X^2 + \sigma_{\hat{X}}^2 + C_2)} \quad (20)$$

$$\text{MAE} = \frac{\|\hat{\mathbf{X}} - \mathbf{X}\|^1}{MN} \quad (21)$$

where $m_Y[j]$, $m_{\hat{X}}[j]$, and $m_X[j]$ are the mean values of the j th striping line in the raw, destriped, and reference images, while m_X and $m_{\hat{X}}$ denote the mean values of the whole images \mathbf{X} and $\hat{\mathbf{X}}$. σ_X and $\sigma_{\hat{X}}$ stand for the variances, and $\sigma_{\mathbf{X}\hat{\mathbf{X}}}$ represents the covariance between \mathbf{X} and $\hat{\mathbf{X}}$. In practice, IF1 was utilized to reflect the image improvement after

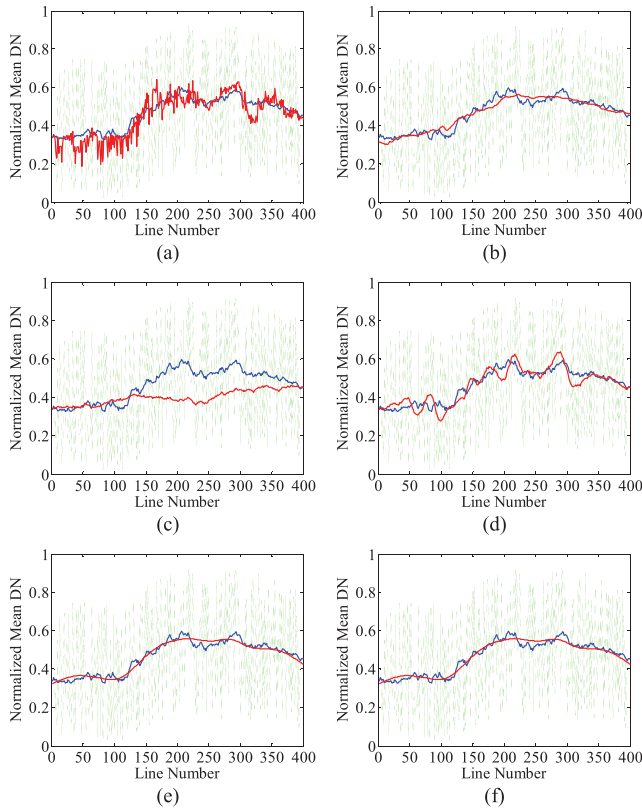


Fig. 7. Mean cross-track profiles of simulated case 1, containing processed (red curve), noisy (green dashed line), and reference (blue curve) profiles. (a) MM. (b) WAFT. (c) UTV. (d) SSC. (e) Proposed method after 1-D filtering. (f) Proposed method after 2-D destriping.

TABLE II

QUANTITATIVE ASSESSMENT OF THE FULL-REFERENCE INDEXES IN THE SIMULATED DATA EXPERIMENTS

Image	Index	MM	WAFT	UTV	SSC	Proposed
Case 1	IF1	13.29	19.44	7.61	16.19	21.41
	PSNR	24.13	26.27	19.92	26.36	27.86
	SSIM	0.86	0.94	0.93	0.93	0.95
	MAE (E-2)	4.45	3.24	7.84	3.49	2.59
Case 2	IF1	6.67	7.29	5.89	5.83	22.09
	PSNR	24.70	25.82	26.36	25.96	37.91
	SSIM	0.92	0.94	0.99	0.96	0.99
	MAE (E-2)	3.85	3.97	4.29	1.77	0.78

destriping, whereas PSNR, SSIM, and MAE were used to evaluate the fidelity between the reference and destriped images. The related results are listed in Table II.

With regard to the nonreference indexes, the inverse coefficient of variation (ICV) [51], [52] embodies the level of stripe noise, and can be further used to assess the destriping performance of a given method. Conversely, the mean relative deviation (MRD) [6], [8] calculates the change of a noise-free region, and thus measures the ability to retain the original healthy information. These indexes are defined as follows:

$$\text{ICV} = \frac{R_m}{R_s} \quad (22)$$

$$\text{MRD} = \frac{1}{MN} \sum_i \frac{|\hat{X}_i - Y_i|}{Y_i} \times 100\% \quad (23)$$

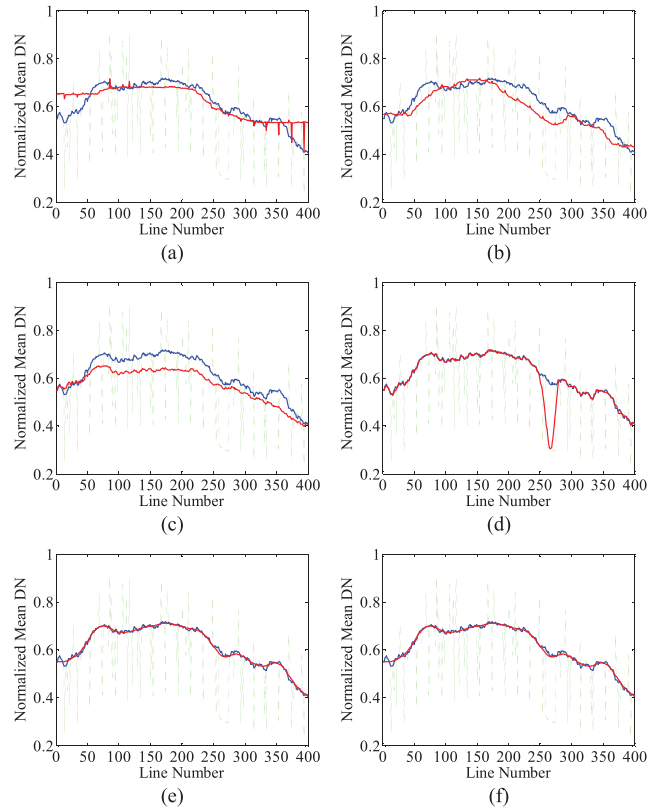


Fig. 8. Mean cross-track profiles of simulated case 2, containing processed (red curve), noisy (green dashed line), and reference (blue curve) profiles. (a) MM. (b) WAFT. (c) UTV. (d) SSC; (e) Proposed method after 1-D filtering. (f) Proposed method after 2-D destriping.

where R_m and R_s denote the mean and standard deviation of a selected image region, and \hat{X}_i and Y_i are the pixel values in the destriped and raw images. In the simulated experiments, the computations of the ICV and MRD indexes were separately done in three sampled 10×10 homogeneous regions and sharp noise-free regions. Due to the absence of a 10×10 noise-free region in simulated case 1, the MRD calculations were just performed in case 2, as displayed in Table III. To give a clear comparison, the top two results for each ICV or MRD sample are labeled in bold, and the underlining denotes their corresponding best values. A better destriping result is reflected by higher IF1, PSNR, SSIM, and ICV values, and lower MAE and MRD values.

Besides being visually the best, the performance of the proposed destriping framework is also quantitatively superior. For example, in Table II, the proposed approach beats the other four methods in all the full-reference evaluations. From the nonreference assessment perspective in Table III, the proposed model also outperforms MM, WAFT, UTV, and SSC, with the most regions of the highest ICV values and the lowest MRD values.

B. Real-Data Experiments

To verify the universality of the proposed method, we also tested the proposed approach on a variety of real data with different types of stripe noise. The test images were

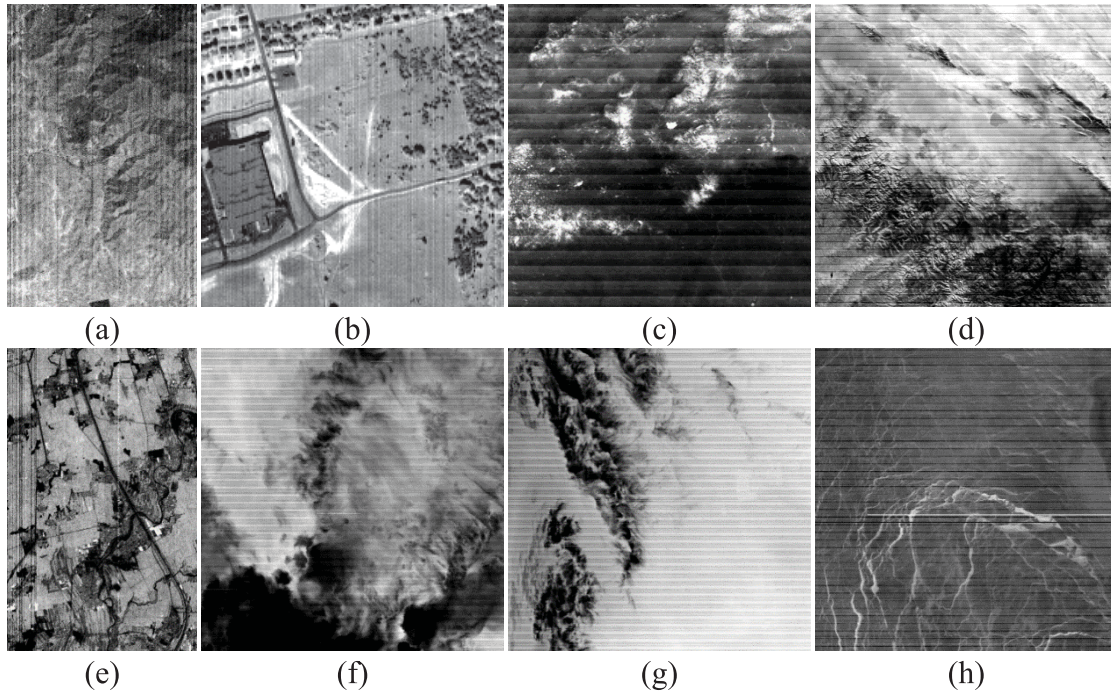


Fig. 9. Experimental images. (a) Hyperion band 8. (b) HYDICE band 103. (c) Aqua MODIS band 16. (d) Aqua MODIS band 30. (e) Hyperion band 56. (f) Terra MODIS band 27. (g) Terra MODIS band 28. (h) Terra MODIS band 30.

TABLE III
QUANTITATIVE ASSESSMENT OF THE NONREFERENCE INDEXES
IN THE SIMULATED DATA EXPERIMENTS

Image	Index	Noisy	MM	WAFT	UTV	SSC	Proposed
Case 1	ICV 1	1.47	14.25	29.94	28.18	30.57	31.71
	ICV 2	2.28	11.73	17.59	20.83	18.78	19.90
	ICV 3	2.54	13.41	16.55	16.95	18.80	21.24
Case 2	ICV 1	12.37	21.10	27.01	27.24	29.37	30.19
	ICV 2	3.27	9.84	34.00	39.05	42.96	41.54
	ICV 3	6.75	17.01	10.91	39.67	43.79	44.56
	MRD 1	-	10.01	8.21	7.81	0.60	0.57
	MRD 2	-	7.01	1.42	10.05	1.06	1.38
	MRD 3	-	3.48	7.48	8.64	0.33	0.28

chosen from several different remote-sensing platforms: one 200×200 Hyperspectral Digital Imagery Collection Experiment (HYDICE) subimage, two 250×400 Hyperion subimages, two 400×400 Aqua MODIS subimages, and three 400×400 Terra MODIS subimages. Fig. 9 provides an overall display of the test data. It is clear that the stripe noise in different images holds distinct features, which basically cover all the possible striping cases introduced in Section I. The detailed striping features in each test image are listed in Table IV. To simplify the parameter setting of the proposed model, p was chosen as $p = 1$ for a sparse striping case and $p = 2$ for a dense striping case. More details of the specific choices of parameters for different data are displayed in the caption of Fig. 10.

Fig. 10 shows the destriping results of the proposed method with all the experimental data, where, most importantly, the results are visually pleasing, without visible residual effects or local distortion. Since the striping cases in the eight test images

are very different, the successful stripe noise removal clearly demonstrates the generic processing ability of the proposed method. Moreover, we also display two examples of the destriping results of the five comparative methods. According to the solutions obtained by MM in Figs. 11(b) and 12(b), its performance can be considered to be worse than all the other methods, with significant remaining stripes. As MM tends to be strongly reliant on the constant linear calibration along one stripe, when faced with more complicated striping cases, like partial stripes, failure becomes inevitable. WAFT, when compared with MM, outputs better destriping results. However, in the magnifications, the residual noise is still nonnegligible, as can be seen in the green rectangle region in Fig. 12(c). The result in Fig. 12(d) indicates that UTV can effectively remove the stripe noise, without apparent remains, whereas the result in Fig. 11(d) reveals the potential oversmoothing of UTV, as the gray “lake” in the green rectangle region is supposed to be black. As for SSC, it can succeed in averting unprocessed residual noise and undue distortion in these two examples, due to the striping sparsity of the test images, which exactly meets its basic modeling assumption. Hence, SSC and the proposed model yield the two best visual performances among the five different methods.

We then drew the mean cross-track profiles of the test data and showed two examples of the results in Figs. 13 and 14. Generally speaking, the mean cross-track profile of an ideal destriping result should be much smoother, but hold a similar curve trend to the profile in the observed image. On the basis of these criteria, MM does a good job in keeping the correct curve trend from the original profile; however, it does not effectively relieve the disturbances. Fig. 14(b) is a typical example. Conversely, UTV gives much smoother profiles in all the results; however, its oversmoothing tendency

TABLE IV
ILLUSTRATION OF THE STRIPING FEATURES IN THE TEST DATA

Image	Direction	Degradation	Distribution	Periodicity	Pattern	Persistence
Hyperion band 8	vertical	warm & dead	local	non-periodic	agminated	integral
HYDICE band 103	vertical	warm	all	non-periodic	single	integral
Aqua band 16	horizontal	warm	all	periodic	banding	integral
Aqua band 30	horizontal	warm	global	periodic	single	integral & partial
Hyperion band 56	vertical	warm & dead	local	non-periodic	single	integral
Terra band 27	horizontal	warm & dead	global	non-periodic	agminated	integral & partial
Terra band 28	horizontal	warm	global	periodic	single	integral
Terra band 30	horizontal	warm & dead	global	non-periodic	single	integral & partial

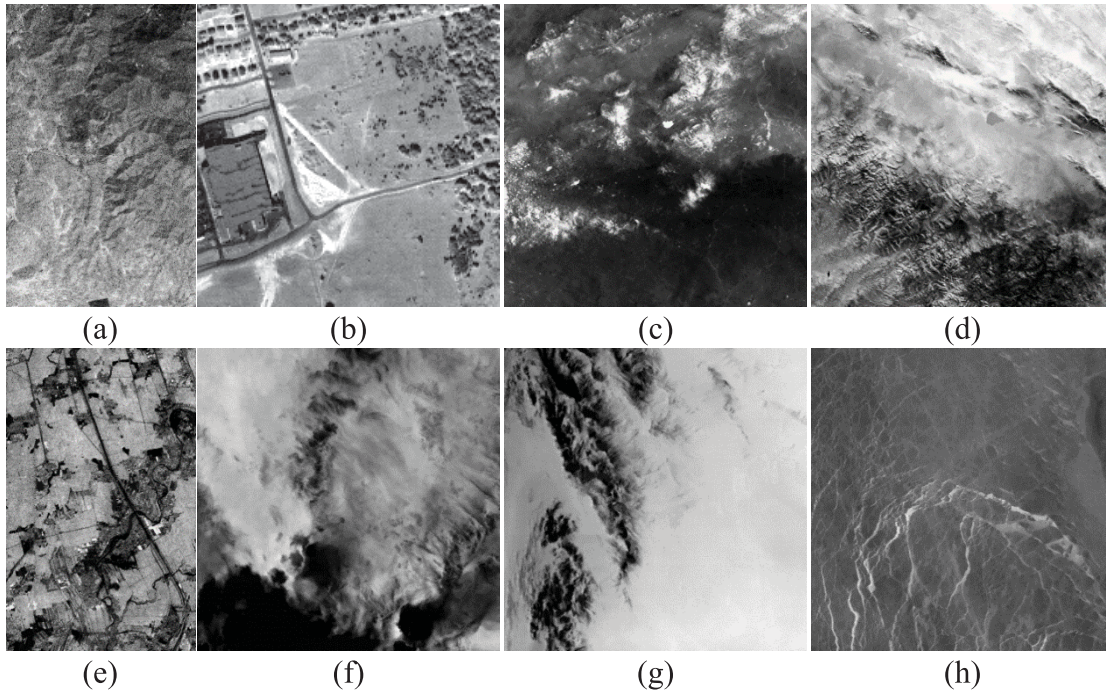


Fig. 10. Destriping results of the proposed method. (a) Hyperion band 8 ($p = 2$, $\lambda = 2000$, and $\lambda_1 = 0.1$). (b) HYDICE band 103 ($p = 1$, $\lambda = 800$, and $\lambda_1 = 0.15$). (c) Aqua MODIS band 16 ($p = 2$, $\lambda = 5000$, and $\lambda_1 = 0.2$). (d) Aqua MODIS band 30 ($p = 1$, $\lambda = 5000$, and $\lambda_1 = 0.15$). (e) Hyperion band 56 ($p = 1$, $\lambda = 2000$, and $\lambda_1 = 0.2$). (f) Terra MODIS band 27 ($p = 2$, $\lambda = 1000$, and $\lambda_1 = 0.2$). (g) Terra MODIS band 28 ($p = 2$, $\lambda = 1000$, and $\lambda_1 = 0.3$). (h) Terra MODIS band 30 ($p = 1$, $\lambda = 2000$, and $\lambda_1 = 0.3$).

significantly decreases the gaps between the maximum and minimum values in some profiles, as shown in Fig. 13(d). Even though the profiles of WAFT in Fig. 14(c) are satisfactory, the unwanted distortion in Fig. 13(c) indicates that the destriping ability of WAFT is unstable. Under the constraint of the sparse assumption, SSC can only alter the stripe-related fluctuations in the mean cross-track profiles as long as they are sparse. Although the sparse constraint is a good fit for sparsely striped data, images with very dense stripe noise can coexist simultaneously. Taking Fig. 9(c) as an example, when “all” the scanning lines are contaminated by stripes, the wrong choice of the first few lines as nonstriping lines adversely affects the destriping performance of SSC, as can be seen in Fig. 14(e). Differing from the above four methods, the proposed model can steadily output reliable and smooth profiles with the correct curve trends. This advantage is remarkable not only for the dense striping [see Fig. 14(f)] but also for the sparse striping cases [see Fig. 13(f)].

For the quantitative assessment in the real-data experiments, two nonreference indexes, ICV and MRD, were used due to the absence of true reference data. Since half of the test images

were affected by random noise (Hyperion band 8, Hyperion band 56, and Terra MODIS band 30) or continuous stripe noise (Aqua MODIS band 16), i.e., their corresponding noise-free regions were almost inexistent, we only computed MRD in the other four images.

Based on the ICV results in Table V, it is apparent that the proposed method obtains the highest values in most of the test regions. Even when the proposed method does not achieve the best ICV value, it almost always obtains the second-best result, with only minor differences. This embodies the stable and superior destriping performance of the proposed model. Only slightly inferior to the proposed framework, UTV and SSC obtain the highest and second-highest ICV values in nearly half of the samples, which means that their destriping capabilities are still competitive. In contrast to the above-mentioned methods, MM and WAFT do not yield satisfactory ICV values in Table V, which is consistent with the visual evaluation in Figs. 11 and 12.

In Table VI, SSC obtains more favorable MRD results (maintaining performance), especially when the stripe noise is sparsely distributed (Aqua MODIS band 30).

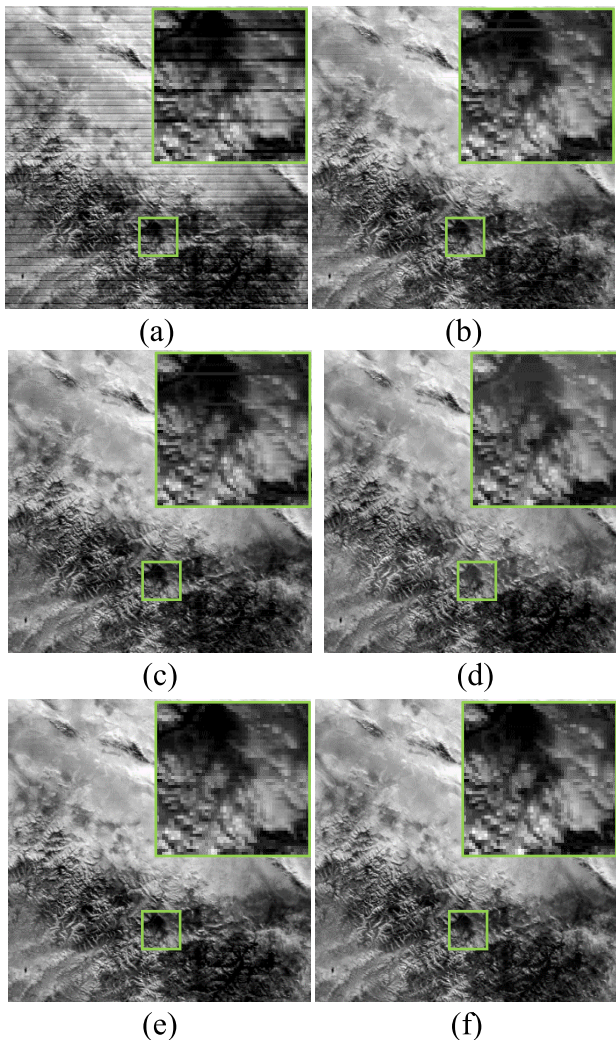


Fig. 11. Destriping results for Aqua MODIS band 30. (a) Original image. (b) MM. (c) WAFT. (d) UTV. (e) SSC. (f) Proposed method.

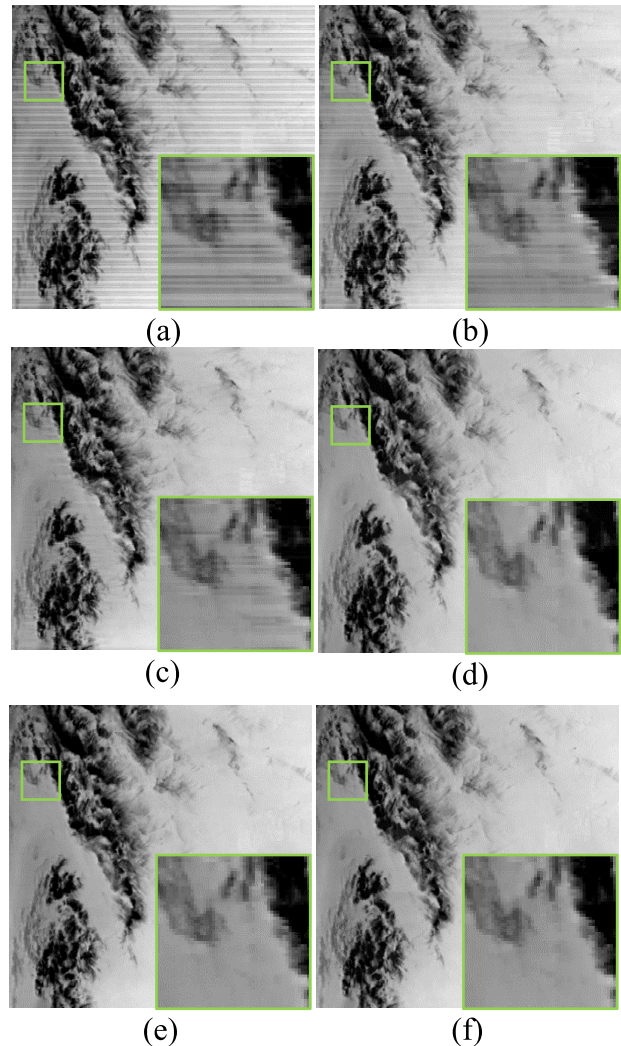


Fig. 12. Destriping results for Terra MODIS band 28. (a) Original image. (b) MM. (c) WAFT. (d) UTV. (e) SSC. (f) Proposed method.

Nevertheless, with the increasing proportion of the stripe noise in the data (HYDICE band 103 and Terra band 28), this advantage decreases significantly, and in Terra MODIS band 27, its superiority is exceeded by the proposed model. Although the proposed approach does not always obtain the best MRD values, the overall results, which outperform MM, WAFT, and UTV, are still remarkable and, most importantly, stable for different kinds of stripes. Since we achieve information maintenance through statistical feature-based guidance, the strength of the proposed approach becomes distinct when processing data with very dense stripes. In such a case, instead of finding the uncertain “healthy pixels” to keep intact, as in SSC, a more rational approach is to first estimate the local statistical features of the latent clean image, and then use them to ensure a reliable destriping process, as in the proposed model.

V. DISCUSSION

A. Parameter Selection

In the first step of profile estimation [see (2)], we use λ to control the smoothness of the curve and p to adapt to

the actual density of stripe distribution. The filtered profile converges to the original data as $\lambda \rightarrow 0$ and to the best affine fit as $\lambda \rightarrow \infty$. For p , a close-to-zero value is theoretically appropriate for an extremely sparse striping case, whereas $p = 2$ can better help in a dense case. Subsequently, in the destriping framework (10), another two parameters exist, λ_1 and λ_2 . As the inner parameter in the anisotropic regularization, parameter λ_1 depends on the actual difference between the across-stripe and along-stripe gradients caused by the stripe noise (which is mainly related to the distribution and pattern). Since the stripe noise can greatly influence the across-stripe gradients, but not the along-stripe gradients in striped images [2], [25], the more severely the stripes damage the across-stripe gradients in \mathbf{Y} , the more helpful a large value of λ_1 will be. Furthermore, parameter λ_2 works to measure the contribution of the statistical feature-based guidance in (10), and a higher λ_2 can introduce more constraint from $G(\mathbf{X})$.

To allow us to give useful guidance for the choice of parameters, we conducted sensitivity analyses of the proposed destriping procedure by taking case 1 and case 2 from the simulated data experiments as examples. Fig. 15 analyzes

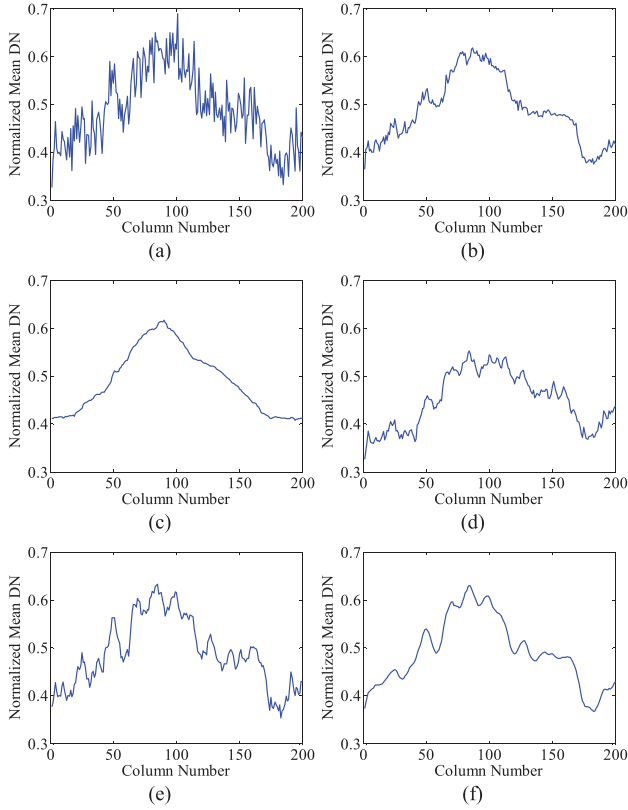


Fig. 13. Mean cross-track profiles of HYDICE band 103. (a) Original image. (b) MM. (c) WAFT. (d) UTV. (e) SSC. (f) Proposed method.

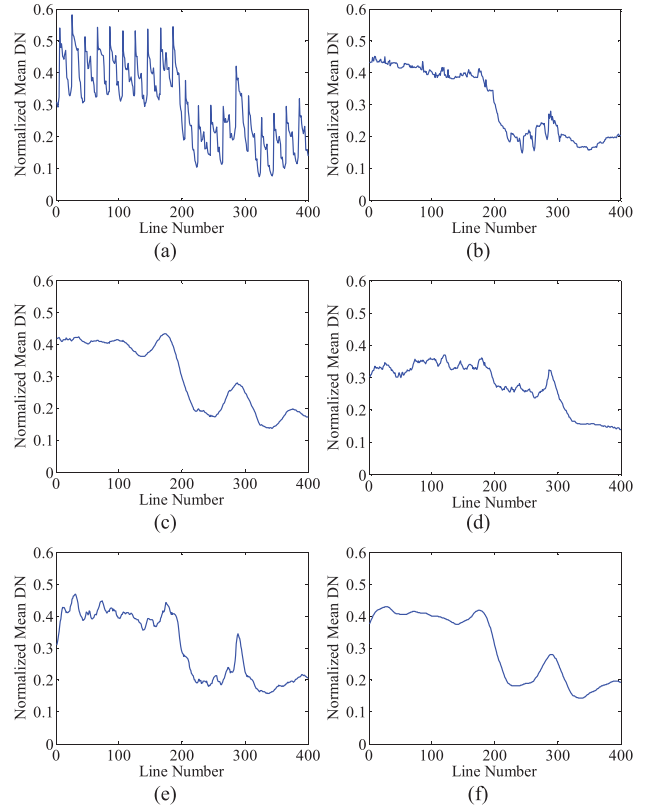


Fig. 14. Mean cross-track profiles of Aqua MODIS band 16. (a) Original image. (b) MM. (c) WAFT. (d) UTV. (e) SSC. (f) Proposed method.

TABLE V
QUANTITATIVE EVALUATION RESULTS USING THE ICV INDEX

Image	Area	Original	MM	WAFT	UTV	SSC	Proposed
Hyperion band 8	Sample 1	3.78	7.80	7.98	7.80	7.85	8.05
	Sample 2	2.57	4.21	4.14	4.00	4.35	4.51
	Sample 3	4.08	5.49	5.60	5.81	5.48	5.61
HYDICE band 103	Sample 1	11.71	16.78	17.43	18.05	18.28	18.34
	Sample 2	10.80	15.56	15.48	16.01	15.77	16.29
	Sample 3	11.99	18.16	18.69	18.91	19.42	19.35
Aqua band 16	Sample 1	1.34	3.10	3.46	4.78	4.43	4.68
	Sample 2	3.95	17.99	15.09	14.38	16.73	20.78
	Sample 3	3.83	6.22	7.52	6.79	9.58	9.24
Aqua band 30	Sample 1	5.50	8.45	8.36	8.28	8.81	9.03
	Sample 2	7.16	18.45	19.74	21.89	21.84	23.40
	Sample 3	6.62	22.31	24.43	21.20	24.94	26.56
Hyperion band 56	Sample 1	3.29	7.50	8.95	7.85	9.35	9.97
	Sample 2	3.09	5.78	7.34	6.75	8.99	9.32
	Sample 3	6.90	9.00	8.16	9.04	8.60	8.73
Terra band 27	Sample 1	12.22	42.84	55.46	65.54	66.25	72.93
	Sample 2	8.47	13.63	18.46	16.50	16.19	18.44
	Sample 3	4.22	5.52	9.65	10.00	10.04	9.73
Terra band 28	Sample 1	11.25	31.17	75.53	94.00	85.88	95.12
	Sample 2	13.00	40.62	79.59	157.10	133.83	154.36
	Sample 3	14.45	62.76	54.65	67.82	66.57	71.82
Terra band 30	Sample 1	5.32	25.32	20.05	26.09	27.47	29.62
	Sample 2	4.24	36.18	34.05	37.48	40.10	40.70
	Sample 3	5.66	19.84	23.06	28.63	26.65	32.38

the effects of p and λ on the correlation coefficient values between the estimated and reference profile [model (2)]. Ideally, the correlation coefficient should be equal to 1. It is

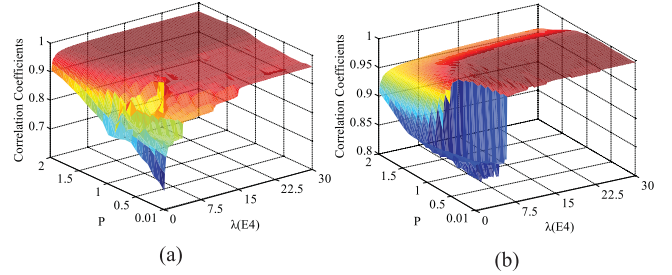


Fig. 15. Sensitivity analysis between parameters p and λ in model (2) using correlation coefficients. (a) Simulated case 1 (dense stripes). (b) Simulated case 2 (sparse stripes).

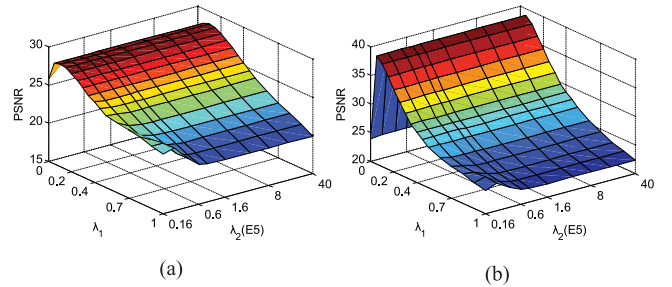


Fig. 16. Sensitivity analysis between parameters λ_1 and λ_2 in model (10) using the PSNR. (a) Simulated case 1 (dense stripes). (b) Simulated case 2 (sparse stripes).

clear that the changes of p only make tiny differences, as can be seen in the relatively high values of λ in the dense striping case when $1 < p \leq 2$ [see Fig. 15(a)] and in the sparse

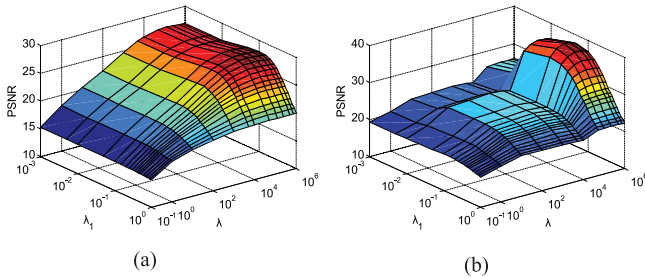


Fig. 17. Sensitivity analysis between parameters λ and λ_1 in the whole destriping process using the PSNR. (a) Simulated case 1 (dense stripes). (b) Simulated case 2 (sparse stripes).

TABLE VI

QUANTITATIVE EVALUATION RESULTS USING THE MRD INDEX (%)

Image	MM	WAFT	UTV	SSC	Proposed
HYDICE band 103	3.25	1.53	9.43	0.37	0.67
Aqua band 30	7.66	7.09	6.36	0.05	6.24
Terra band 27	2.76	4.12	8.34	2.08	2.00
Terra band 28	8.75	9.38	10.80	3.55	3.80

striping case when $0 < p \leq 1$ [see Fig. 15(b)]. Therefore, p should be greater than 1 for a dense case and less than 1 for a sparse case. Considering that the cost function of model (2) is nonconvex for $p < 1$ and the performance of p is stable in the suitable interval, we finally let p become a “binary” parameter, with $p = 1$ for a sparse striping case and $p = 2$ for a dense striping case. Similarly, Fig. 16 shows the result of the PSNR varying with λ_1 and λ_2 [model (10)]. Although the PSNR changes obviously with different values of λ_1 in Fig. 16, the robustness of λ_2 is very satisfying. Since $(\lambda_2/2)\|\hat{\mathbf{g}}(\mathbf{Y}) - \mathbf{X}\mathbf{f}\|_2^2$ is closely related to the length of the guided profile (image rows m), to keep the consistency of the image scale, we should also consider the image columns n . Thus, in all our implementations, we fixed the most insensitive parameter λ_2 as $\lambda_2 = 1000 \times n$ to simplify the parameter setting. As we set p a “binary” parameter and fix $\lambda_2 = 1000 \times n$ in the proposed destriping model, the only parameters to tune are λ and λ_1 . Fig. 17 then displays the effects of different values with respect to these two parameters on the whole destriping performance. Although the best parameter ranges to obtain the satisfying results may be different in different cases, the relatively stable PSNR performance in the certain order of magnitude of λ and λ_1 will make the parameter selection much easier and more convenient. Empirically, λ and λ_1 were separately chosen from the range of $[500, 500000]$ and $[0.1, 1]$.

For the parameters in the mathematical solutions, α in IRLS was fixed as 10^{-5} and the penalty parameters ρ_1 and ρ_2 in ADMM were also fixed as $\rho_1 = \rho_2 = 5$. For the parameters in the other four comparative methods, their selection in all the experiments was based on the recommendations of the corresponding publications. However, for the purpose of attaining the best visual performance in the real implementations, we did some further adjustments.

TABLE VII

RUNNING TIMES (S) OF DIFFERENT METHODS WITH DIFFERENT IMAGE SIZES

Image size	MM	WAFT	UTV	SSC	Proposed
200×200	0.06	0.19	4.58	0.95	0.94
400×400	0.10	0.23	42.10	5.94	5.88
2030×1354	0.77	1.29	369.45	98.35	99.78

B. Running Time

In the proposed destriping procedure, the guidance $\hat{\mathbf{g}}(\mathbf{Y})$ can be efficiently estimated within a second through the IRLS method for $p = 1$ in model (2). For $p = 2$, the estimation is even easier, since, in this case, the solution of $\hat{\mathbf{g}}(\mathbf{Y})$ becomes a linear system, which can be directly solved by the least-squares method. In practice, all the IRLS implementations will stop when the relative change in $\hat{\mathbf{g}}(\mathbf{Y})$ becomes less than 10^{-5} , or when the calculation reaches the maximum iteration number as 50. Concerning the relatively complex destriping model in (10), it can be split into three simpler subproblems through the ADMM framework. The \mathbf{H} and \mathbf{V} subproblems are solved via a fast shrinkage operator in parallel, while the quadratic minimization problem of \mathbf{X} in (16) is accelerated by the extremely efficient FFT. The updating of the two Lagrange multipliers p_1 and p_2 in (17) is also undertaken in parallel, which further eases the calculation load of the proposed method. The running times of the five methods are compared in Table VII. Although UTV, SSC, and the proposed method are all solved by the ADMM framework in our test, the lack of help from FFT clearly increases the computation time of UTV. To verify the usability of the proposed method for large-swath remote-sensing images, a real MODIS image of 2030×1354 was also tested. Without any large-swath data based acceleration strategy, the whole running time of about 1.5 min for the proposed model is still acceptable for real applications. On the condition that all the experiments were conducted in MATLAB on a desktop personal computer with a 3.4-GHz CPU and 8-GB RAM, the proposed method could be further accelerated using optimized C or the block processing technique.

C. Guided Profile Acquisition

To attain the best profile $\hat{\mathbf{g}}(\mathbf{Y})$, we designed a robust but an effective filter that can not only estimate an accurate curve trend from a noisy data series, but is also adept in adaptively controlling the processing degree for different striping cases. Under the assumption that the locations of the striping lines in the test data are unknown, when filtering the original mean cross-track profiles, we do not consider the question as to whether or not the fluctuations in the 1-D consecutive noisy signal match the natural disturbances or striping occurrences. However, if the locations of the stripe noise are available in advance, for an accurate estimation, a theoretically more suitable approach is to first mark the stripe-related fluctuations, and then alleviate them without changing the natural disturbances. Of course, this is another task, which is beyond the scope of this paper. Since the acquisition of stripe location

information is challenging and meaningful, we will consider this issue in our future research work.

VI. CONCLUSION

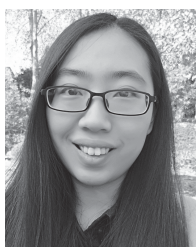
In this paper, we have proposed a generic destriping model using the 1-D statistical property to guide and control the 2-D estimation of clean images. To ensure the accuracy of the guidance information, a 1-D variational model (modified HP filter) is proposed. The efficient IRLS method and ADMM are both applied in the proposed destriping procedure to solve and accelerate the minimization problems. Data covering nearly all different striping features were tested in the experiments. Both the qualitative and quantitative results confirmed the excellent universality and stability of the proposed model when compared with the other four approaches of MM, WAFT, UTV, and SSC.

Although the proposed destriping framework is robust to most of the stripe types that exist in remote-sensing images without georectification, potential oblique stripe noise is still a challenge. In order to further upgrade the universality of the proposed destriping model, we will attempt to consider the specific direction of the stripe noise and incorporate this information in the stripe removal in our future work.

REFERENCES

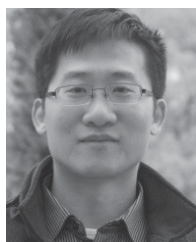
- [1] H. Carfantan and J. Idier, "Statistical linear destriping of satellite-based pushbroom-type images," *IEEE Trans. Geosci. Remote Sens.*, vol. 48, no. 4, pp. 1860–1871, Apr. 2010.
- [2] M. Bouali and S. Ladjal, "Toward optimal destriping of MODIS data using a unidirectional variational model," *IEEE Trans. Geosci. Remote Sens.*, vol. 49, no. 8, pp. 2924–2935, Aug. 2011.
- [3] P. Rakwatin, W. Takeuchi, and Y. Yasuoka, "Stripe noise reduction in MODIS data by combining histogram matching with facet filter," *IEEE Trans. Geosci. Remote Sens.*, vol. 45, no. 6, pp. 1844–1856, Jun. 2007.
- [4] N. Acito, M. Diani, and G. Corsini, "Subspace-based striping noise reduction in hyperspectral images," *IEEE Trans. Geosci. Remote Sens.*, vol. 49, no. 4, pp. 1325–1342, Apr. 2011.
- [5] N. Acito, M. Diani, and G. Corsini, "Residual striping reduction in hyperspectral images," in *Proc. 17th Int. Conf. Digit. Signal Process.*, Jul. 2011, pp. 1–7.
- [6] H. Shen and L. Zhang, "A MAP-based algorithm for destriping and inpainting of remotely sensed images," *IEEE Trans. Geosci. Remote Sens.*, vol. 47, no. 5, pp. 1492–1502, May 2009.
- [7] B. M. Ratliff, J. S. Tyo, J. K. Boger, W. T. Black, D. L. Bowers, and M. P. Fetrow, "Dead pixel replacement in LWIR microgrid polarimeters," *Opt. Exp.*, vol. 15, no. 12, pp. 7596–7609, Jun. 2007.
- [8] Y. Chang, L. Yan, H. Fang, and C. Luo, "Anisotropic spectral-spatial total variation model for multispectral remote sensing image destriping," *IEEE Trans. Image Process.*, vol. 24, no. 6, pp. 1852–1866, Jun. 2015.
- [9] H.-S. Jung, J.-S. Won, M.-H. Kang, and Y.-W. Lee, "Detection and restoration of defective lines in the SPOT 4 SWIR band," *IEEE Trans. Image Process.*, vol. 19, no. 8, pp. 2143–2156, Aug. 2010.
- [10] A. D. Fischer, T. J. Thomas, R. A. Leathers, and T. V. Downes, "Stable scene-based non-uniformity correction coefficients for hyperspectral SWIR sensors," in *Proc. IEEE Aerosp. Conf.*, Mar. 2007, pp. 1–14.
- [11] G. Corsini, M. Diani, and T. Walzel, "Striping removal in MOS-B data," *IEEE Trans. Geosci. Remote Sens.*, vol. 38, no. 3, pp. 1439–1446, May 2000.
- [12] R. Bindschadler and H. Choi, "Characterizing and correcting Hyperion detectors using ice-sheet images," *IEEE Trans. Geosci. Remote Sens.*, vol. 41, no. 6, pp. 1189–1193, Jun. 2003.
- [13] J. Chen, Y. Shao, H. Guo, W. Wang, and B. Zhu, "Destriping CMODIS data by power filtering," *IEEE Trans. Geosci. Remote Sens.*, vol. 41, no. 9, pp. 2119–2124, Sep. 2003.
- [14] J.-J. Pan and C.-I. Chang, "Destriping of Landsat MSS images by filtering techniques," *Photogramm. Eng. Remote Sens.*, vol. 58, no. 10, pp. 1417–1423, 1992.
- [15] J. Torres and S. O. Infante, "Wavelet analysis for the elimination of striping noise in satellite images," *Opt. Eng.*, vol. 40, no. 7, pp. 1309–1314, Jul. 2001.
- [16] J. S. Chen, H. Lin, Y. Shao, and L. Yang, "Oblique striping removal in remote sensing imagery based on wavelet transform," *Int. J. Remote Sens.*, vol. 27, no. 8, pp. 1717–1723, Apr. 2006.
- [17] B. Münch, P. Trtik, F. Marone, and M. Stapanoni, "Stripe and ring artifact removal with combined wavelet—Fourier filtering," *Opt. Exp.*, vol. 17, no. 10, pp. 8567–8591, May 2009.
- [18] R. Pande-Chhetri and A. Abd-Elrahman, "De-striping hyperspectral imagery using wavelet transform and adaptive frequency domain filtering," *ISPRS J. Photogramm. Remote Sens.*, vol. 66, no. 5, pp. 620–636, Sep. 2011.
- [19] F. Tsai and W. W. Chen, "Striping noise detection and correction of remote sensing images," *IEEE Trans. Geosci. Remote Sens.*, vol. 46, no. 12, pp. 4122–4131, Dec. 2008.
- [20] F. L. Gadallah, F. Csillag, and E. J. M. Smith, "Destriping multisensor imagery with moment matching," *Int. J. Remote Sens.*, vol. 21, no. 12, pp. 2505–2511, Aug. 2000.
- [21] V. R. Algazi and G. E. Ford, "Radiometric equalization of nonperiodic striping in satellite data," *Comput. Graph. Image Process.*, vol. 16, no. 3, pp. 287–295, Jul. 1981.
- [22] B. K. P. Horn and R. J. Woodham, "Destriping LANDSAT MSS images by histogram modification," *Comput. Graph. Image Process.*, vol. 10, no. 1, pp. 69–83, May 1979.
- [23] M. Wegener, "Destriping multiple sensor imagery by improved histogram matching," *Int. J. Remote Sens.*, vol. 11, no. 5, pp. 859–875, May 1990.
- [24] H. Shen, W. Jiang, H. Zhang, and L. Zhang, "A piece-wise approach to removing the nonlinear and irregular stripes in MODIS data," *Int. J. Remote Sens.*, vol. 35, no. 1, pp. 44–53, Nov. 2013.
- [25] Y. Chang, L. Yan, H. Fang, and H. Liu, "Simultaneous destriping and denoising for remote sensing images with unidirectional total variation and sparse representation," *IEEE Geosci. Remote Sens. Lett.*, vol. 11, no. 6, pp. 1051–1055, Jun. 2014.
- [26] X. Liu, X. Lu, H. Shen, Q. Yuan, Y. Jiao, and L. Zhang, "Stripe noise separation and removal in remote sensing images by consideration of the global sparsity and local variational properties," *IEEE Trans. Geosci. Remote Sens.*, vol. 54, no. 5, pp. 3049–3060, May 2016.
- [27] X. Liu, H. Shen, Q. Yuan, L. Zhang, and Q. Cheng, "A novel removal method for dense stripes in remote sensing images," in *Proc. ISPRS, Prague, Czech Republic*, 2016, pp. 57–61.
- [28] Y. Yuan, X. Zheng, and X. Lu, "Discovering diverse subset for unsupervised hyperspectral band selection," *IEEE Trans. Image Process.*, vol. 26, no. 1, pp. 51–64, Jan. 2017.
- [29] X. Lu, H. Wu, Y. Yuan, P. Yan, and X. Li, "Manifold regularized sparse NMF for hyperspectral unmixing," *IEEE Trans. Geosci. Remote Sens.*, vol. 51, no. 5, pp. 2815–2826, May 2013.
- [30] H. Shen, X. Meng, and L. Zhang, "An integrated framework for the spatio-temporal-spectral fusion of remote sensing images," *IEEE Trans. Geosci. Remote Sens.*, vol. 54, no. 12, pp. 7135–7148, Dec. 2016.
- [31] L. Sun, R. Neville, K. Staenz, and H. P. White, "Automatic destriping of Hyperion imagery based on spectral moment matching," *Can. J. Remote Sens.*, vol. 34, no. S1, pp. S68–S81, Jan. 2008.
- [32] X. Lu, Y. Wang, and Y. Yuan, "Graph-regularized low-rank representation for destriping of hyperspectral images," *IEEE Trans. Geosci. Remote Sens.*, vol. 51, no. 7, pp. 4009–4018, Jul. 2013.
- [33] H. Zhang, W. He, L. Zhang, H. Shen, and Q. Yuan, "Hyperspectral image restoration using low-rank matrix recovery," *IEEE Trans. Geosci. Remote Sens.*, vol. 52, no. 8, pp. 4729–4743, Aug. 2014.
- [34] X. Lu, H. Wu, and Y. Yuan, "Double constrained NMF for hyperspectral unmixing," *IEEE Trans. Geosci. Remote Sens.*, vol. 52, no. 5, pp. 2746–2758, May 2014.
- [35] Y. Yuan, M. Fu, and X. Lu, "Substance dependence constrained sparse NMF for hyperspectral unmixing," *IEEE Trans. Geosci. Remote Sens.*, vol. 53, no. 6, pp. 2975–2986, Jun. 2015.
- [36] D. Cerra, R. Müller, and P. Reinartz, "Unmixing-based denoising for destriping and inpainting of hyperspectral images," in *Proc. IEEE Geosci. Remote Sens. Symp.*, Jul. 2014, pp. 4620–4623.
- [37] R. J. Hodrick and E. C. Prescott, "Postwar U.S. business cycles: An empirical investigation," *J. Money, Credit, Banking*, vol. 29, no. 1, pp. 1–16, Feb. 1997.
- [38] A. Maravall and A. del Río, "Temporal aggregation, systematic sampling, and the Hodrick–Prescott filter," *Comput. Statist. Data Anal.*, vol. 52, no. 2, pp. 975–998, Oct. 2007.
- [39] S.-J. Kim, K. Koh, S. Boyd, and D. Gorinevsky, " ℓ_1 trend filtering," *SIAM Rev.*, vol. 51, no. 2, pp. 339–360, Apr. 2009.

- [40] R. J. Tibshirani, "Adaptive piecewise polynomial estimation via trend filtering," *Ann. Statist.*, vol. 42, no. 1, pp. 285–323, Mar. 2014.
- [41] P. Rodriguez and B. Wohlberg, "Efficient minimization method for a generalized total variation functional," *IEEE Trans. Image Process.*, vol. 18, no. 2, pp. 322–332, Feb. 2009.
- [42] H. Shen, L. Peng, L. Yue, Q. Yuan, and L. Zhang, "Adaptive norm selection for regularized image restoration and super-resolution," *IEEE Trans. Cybern.*, vol. 46, no. 6, pp. 1388–1399, Jun. 2016.
- [43] L. I. Rudin, S. Osher, and E. Fatemi, "Nonlinear total variation based noise removal algorithms," *Phys. D, Nonlinear Dyn.*, vol. 60, nos. 1–4, pp. 259–268, Nov. 1992.
- [44] Q. Yuan, L. Zhang, and H. Shen, "Hyperspectral image denoising employing a spectral–spatial adaptive total variation model," *IEEE Trans. Geosci. Remote Sens.*, vol. 50, no. 10, pp. 3660–3677, Oct. 2012.
- [45] H. Shen *et al.*, "Missing information reconstruction of remote sensing data: A technical review," *IEEE Geosci. Remote Sens. Mag.*, vol. 3, no. 3, pp. 61–85, Sep. 2015.
- [46] S. Boyd, N. Parikh, E. Chu, B. Peleato, and J. Eckstein, "Distributed optimization and statistical learning via the alternating direction method of multipliers," *Found. Trends Mach. Learn.*, vol. 3, no. 1, pp. 1–122, Jan. 2011.
- [47] D. L. Donoho, "De-noising by soft-thresholding," *IEEE Trans. Inf. Theory*, vol. 41, no. 3, pp. 613–627, May 1995.
- [48] P. C. Hansen, J. G. Nagy, and D. P. O'Leary, *Deblurring Images: Matrices, Spectra, and Filtering*. Philadelphia, PA, USA: SIAM, 2006, pp. 33–54.
- [49] Z. Wang, A. C. Bovik, H. R. Sheikh, and E. P. Simoncelli, "Image quality assessment: From error visibility to structural similarity," *IEEE Trans. Image Process.*, vol. 13, no. 4, pp. 600–612, Apr. 2004.
- [50] Z. Wang and A. C. Bovik, "Mean squared error: Love it or leave it? A new look at signal fidelity measures," *IEEE Signal Process. Mag.*, vol. 26, no. 1, pp. 98–117, Jan. 2009.
- [51] G. Smith and P. Curran, "Methods for estimating image signal-to-noise ratio (SNR)," in *Advances in Remote Sensing and GIS Analysis*, P. Atkinson and N. Tate, Eds. Hoboken, NJ, USA: Wiley, 2000, pp. 61–74.
- [52] J. E. Nichol and V. Vohora, "Noise over water surfaces in Landsat TM images," *Int. J. Remote Sens.*, vol. 25, no. 11, pp. 2087–2093, Jun. 2004.



Xinxin Liu received the B.S. degree in geographic information system from Wuhan University, Wuhan, China, in 2013, where she is currently pursuing the Ph.D. degree with the School of Resource and Environmental Sciences.

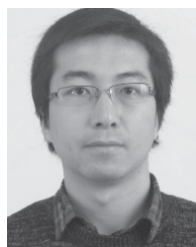
Her research interests include image quality improvement and remote-sensing image processing.



Huanfeng Shen (M'10–SM'13) received the B.S. degree in surveying and mapping engineering and the Ph.D. degree in photogrammetry and remote sensing from Wuhan University, Wuhan, China, in 2002 and 2007, respectively.

In 2007, he joined the School of Resource and Environmental Sciences, Wuhan University, where he is currently a Luojia Distinguished Professor. He has authored over 100 research papers. His research interests include image quality improvement, remote-sensing mapping and application, data fusion and assimilation, and regional and global environmental change.

Dr. Shen is currently a member of the editorial board of the *Journal of Applied Remote Sensing*. He has been supported by several talent programs, such as the Youth Talent Support Program of China (2015), China National Science Fund for Excellent Young Scholars (2014), and the New Century Excellent Talents by the Ministry of Education of China (2011).



Qiangqiang Yuan (M'13) received the B.S. degree in surveying and mapping engineering and the Ph.D. degree in photogrammetry and remote sensing from Wuhan University, Wuhan, China, in 2006 and 2012, respectively.

In 2012, he joined the School of Geodesy and Geomatics, Wuhan University, where he is currently an Associate Professor. He has frequently served as a Referee of over ten international journals for remote sensing and image processing. He has authored over 30 research papers, including more than 20 peer-reviewed articles in international journals such as the *IEEE TRANSACTIONS ON IMAGE PROCESSING* and the *IEEE TRANSACTIONS ON GEOSCIENCE AND REMOTE SENSING*. His research interests include image reconstruction, remote-sensing image processing and application, and data fusion.

Dr. Yuan was a recipient of the Top-Ten Academic Star of Wuhan University in 2011. In 2014, he received the Hong Kong Scholar Award from the Society of Hong Kong Scholars and the China National Postdoctoral Council.



Xiliang Lu received the B.S. degree in computational mathematics from Peking University, Beijing, China, in 2000, and the Ph.D. degree in computational mathematics from the National University of Singapore, Singapore, in 2006.

He is currently a Professor with the School of Mathematics and Statistics, Wuhan University, Wuhan, China. His research interests include computational inverse problems and their applications.



Chunping Zhou received the B.S. degree in surveying and mapping from Dalian Naval Academy, Dalian, China, in 1987, the M.S. degree in cartography and remote sensing from Peking University, Beijing, China, in 1992, and the Ph.D. degree in geography from the Chinese Academy of Sciences, Beijing, in 1996.

He is currently a Professor with Capital Normal University, Beijing. His research interests include remote sensing and image processing.